Modulating Lattice Oxygen Activity of $Ca_2Fe_2O_5$ Brownmillerite for the Co-production of Syngas and High Purity Hydrogen via Chemical Looping Steam Reforming of Toluene

Tingting Xu[a,b,c,d], Xun Wang[a*], Haibo zhao[b], Bo Xiao[a], Dong Liu[c,d], Wen Liu[e,f*]

[a] School of Environmental Science & Engineering, Huazhong University of Science & Technology, Wuhan 430074, China.

[b] State Key Laboratory of Coal Combustion, Huazhong University of Science & Technology, Wuhan 430074, China.

[c] MIIT Key Laboratory of Thermal Control of Electronic Equipment, School of Energy and Power Engineering, Nanjing University of Science and Technology, Nanjing 210094, China.

[d] Advanced Combustion Laboratory, School of Energy and Power Engineering, Nanjing University of Science and Technology, Nanjing 210094, China.

[e] School of Chemical and Biomedical Engineering, Nanyang Technological University, 62 Nanyang Drive, Singapore 637459, Singapore.

[f] Cambridge Centre for Advanced Research and Education, 1 CREATE Way, Singapore 138602, Singapore.

Abstract

The chemical looping steam reforming (CLSR) of biomass tar enables the process intensification for the co-preparation of syngas and high purity hydrogen. The practical application of brownmillerite-structured $Ca_2Fe_2O_5$ is hindered by activity-related issues such as low fuel conversion and oxygen transfer capacity. Here, the doping of heteroatoms, e.g. Ni induces structural changes to the brownmillerite lattice, transforming it from a *Pnma* phase to a *Pcmn* one, with increased distortion of the FeO_6 octahedra. The structural changes lead to the upwards shifts of the O 2*p* band of oxygen carrier, and subsequently improved lattice oxygen activity as well as oxygen transfer capacity. The formation of oxygen vacancy is a rate determining step during CLSR, while the Ni-doped $Ca_2Fe_2O_5$ reduces the energy of oxygen vacancy formation and

---

* Corresponding authors: E-mail addresses: xunw@hust.edu.cn (Xun Wang); wenliu@ntu.edu.sg (Wen Liu); Mail to: xunw@hust.edu.cn (Xun Wang)

energy barrier for lattice oxygen migration through the bulk. During CLSR, $Ca_2Ni_{0.25}Fe_{1.75}O_5$ lead to significant improvement in syngas productivity, hydrogen purity and fuel conversion.

Key words:

Brownmillerite; Lattice oxygen activity; Chemical looping reforming; Syngas; Hydrogen;

1 Introduction

Hydrogen energy has the advantages of large reserves, no pollution, energy per unit mass is 3 times of petroleum, 4-5 times of coal, wide application scenarios. However, at present, the hydrogen production industry is facing problems such as dependence on fossil energy technology and serious carbon emissions. The development of low-carbon hydrogen production technology is the current research focus. The chemical looping steam reforming (CLSR) is proposed as a promising technology for the co-production syngas (mixture of H_2 and CO) and high purity H_2 in one route [1]. Compared with the traditional thermochemical hydrogen production from biomass, no segregation equipment is needed for the CLSR. When the carbon neutral feedstocks, e.g. those derived from biomass and bio-waste are used as the fuel, CLSR could be employed to realize the production of carbon-negative hydrogen [2, 3].

During CLSR, biomass is partially oxidases in the fuel reactor (FR) by the lattice oxygen of an oxygen carrier. After depletion of its redox-active lattice oxygen, the reduced oxygen carrier thermochemically reduces steam in the steam reactor (SR), producing hydrogen. Given that the reactions in both reactors involve the oxygen carrier, the design of the oxygen carrier is critical to the overall productivity, selectivity and efficiency of the CLSR process [4]. In terms of performance, an ideal oxygen carrier for CLSR should: (i) oxidise biomass in the fuel reactor with high syngas selectivity; (ii) high oxygen transfer capacity; (iii) efficiently reduce water to H_2 in the steam reactor [5]. In fact, the redox properties described above depend on the crystalline phase, chemical composition and the surface structures of the metal oxides (i.e. oxygen carriers) [1]; changing any of the parameters could result in drastic changes to the coordination environment of the transition metal centres (both on the surface or in the bulk), the electronic structures of the oxygen carriers and ultimately their redox activities. For perovskites-structured oxygen carriers, the relationships between oxide carrier formulation and their redox functionalities have been extensively studied [6, 7]. For instance, Gong and co-workers [8] showed that modulating the degree of distortion of BO_6 octahedral in a perovskites-structured $LaFeO_3$ by Ce doping could tune the selectivity of the lattice oxygen between methane combustion and methane partial oxidation under a chemical looping scheme. Wang and co-workers [9] reported that the A-site doping of $La_{1-x}Sr_xFe_{0.8}Al_{0.2}O_3$ perovskite significantly increased the oxygen capacity and the amount of oxygen vacancy, whilst suppressing coke deposition during chemical looping methane to syngas process. Yinlong Zhu et al. [10] reported a facile A/B-site co-substitution strategy oxide to regulate the electronic structure of oxygen-deficient brownmillerite oxides $CaSrCoFeO_{6-\delta}$ for optimizing the oxygen evolution reaction (OER) performance.

Recent researches have also shown that, the brownmillerite-structured $Ca_2Fe_2O_5$ possesses suitable properties for CLSR, including good syngas selectivity and the ability to produce relatively high partial pressure of hydrogen in the steam reactor [11]. On the other hand, $Ca_2Fe_2O_5$ has low oxygen transfer capacity (OTC) and is susceptible to low fuel conversion in the fuel reactor. Therefore, further development is required to improve the chemical looping performance of brownmillerite, including modulating the lattice oxygen activity and incorporating catalytic activity to the surface of the brownmillerite. In fact, studies have shown that A/B-site doping could alter the lattice oxygen activity of $A_2B_2O_5$ brownmillerite oxides. The A site is typically occupied by large metal ions, such as Ca, Sr, Ba and lanthanides, whereas B sites are occupied by 3d transition metals ions or those with comparable ionic radii (e.g. Al^{3+}). For example, Liu et al. [12, 13] found that both Sr and Co doping to $Ca_2Fe_2O_5$ promoted the syngas selectivity of chemical looping microalgae gasification, and a suitable doping content of < 0.5 is significant for the gas production selectivity. Müller and co-workers [14] studied CLSR of methane using $Ca_2Fe_2O_5$ doped with 5wt.% Ni to $Ca_2Fe_2O_5$ and reported that the Ni-doped $Ca_2Fe_2O_5$ showed significantly improved H_2 yield over 15 CLSR cycles of unmodified $Ca_2Fe_2O_5$, despite its cyclic deactivation. Although the literature ubiquitously reports favorable consequences of heteroatom doping to $Ca_2Fe_2O_5$. The underlaying origin of the promotional affect due to doping remain in sufficiently explained.

During biomass pyrolysis, the tar produced has complex composition, including toluene (~24%), naphthalene (1~5%) and other monocyclic (22%) and bicyclic (~13%) aromatic hydrocarbons [15], which could not be easily upgraded. Therefore, the most practical method of valorizing tar compounds is to thermochemically decompose them to syngas, e.g. by CLSR. In order to improve the accuracy of the analysis (e.g. for closing the carbon balance), toluene and naphthalene are commonly used as model compounds to simulate biomass tar [3, 15], where the former is in liquid form at ambient condition and therefore much easier to work with during feeding and product separation than naphthalene. In this study, we prepared Ni-doped brownmillerite oxides with general formulae of $Ca_2Ni_xFe_{2-x}O_5$ ($x = 0, 0.25, 0.5, 0.75$ and 1), to investigate the role of B-site doping for CLSR of toluene to produce syngas and high-purity hydrogen. Here, toluene represents a model aromatic component in biomass tar, a byproduct of biomass pyrolysis. Through a systematic investigation, we found that Ni doping induced structural changes to the brownmillerite phase, promoting the formation of surface oxygen vacancy and the migration of bulk lattice oxygen, both appeared beneficial to improving fuel conversion and enhancing oxygen transfer capacity. Density functional theory (DFT) calculations reveal that the energy of oxygen vacancy formation and bulk oxygen migration reduce from 2.38 eV to 1.45 eV and 0.64 eV to 0.27 eV upon doping Ni to $Ca_2Fe_2O_5$. Amongst the Ni-doped brownmillerite samples,

$Ca_2Ni_{0.5}Fe_{1.5}O_5$ shows the most oxygen vacancy and the best CLSR performance in terms of the concentration and amount of syngas produced in FR, the purity and amount of H_2 produced in SR, with both reactors operated at 900 °C and an oxygen supply coefficient of 1.

2 Experiment and characterization

2.1 Oxygen carrier preparation

The $Ca_2Ni_xFe_{2-x}O_5$ (x = 0, 0.25, 0.5, 0.75, 1) oxygen carriers with different Ni doping contents in B site are prepared by the sol−gel method. Typically, the required amounts of $Fe(NO_3)_3{\cdot}9H_2O$, $Ca(NO_3)_2{\cdot}4H_2O$, $Ni(NO_3)_2{\cdot}6H_2O$ and $C_6H_8O_7{\cdot}H_2O$ (citric acid) are dissolved in deionized water to obtain a homogeneous solution. The molar ratio of citric acid to total metal ion is 1.5. The homogeneous solution is slowly stirred at 95 °C until a viscous gel observed. Then the gel is transferred to a drying oven at 105 °C until the sample is completely dried. After that, the sample is calcined in a muffle furnace at 1,000 °C for 10 h under atmospheric condition. Finally, the naturally cooled sample is ground and sieved to the size range of < 212 μm (70 meshes) for characterization and toluene reforming experiments. The as-prepared Ni modified oxygen carriers, $Ca_2Ni_xFe_{2-x}O_5$, were expressed as NixFe2-x. For example, the $Ca_2Ni_{0.5}Fe_{1.5}O_5$ is expressed as Ni0.50Fe1.50.

As a control experiment, NiO is doped to pre-synthesised $Ca_2Fe_2O_5$ by means of mechanical mixing. NiO is a commercially available reagent (CAS No.: 1313-99-1) with a purity of 99.9% metals basis and size of 50 nm, respectively. $Ca_2Fe_2O_5$ is the oxygen carrier of undoped nickel described above. NiO and $Ca_2Fe_2O_5$ are thoroughly mixed in mortar and heated in a muffle furnace for 1 hour at 1,000 °C, in which the molar ratio of nickel to iron is 0.25/1.75. The sample is denoted $NiO/Ca_2Fe_2O_5$.

2.2 The fixed bed experiments

Chemical looping steam toluene reforming experiments are conducted in a lab-scale fixed bed reactor, as schematically illustrated in Figure S1. Details of the apparatus can be found in our previous papers [16] and are briefly described as follows. The reactor system consists of gas feed, a toluene injection pump and a steam injection pump. The fixed bed reactor is made of a quartz tube (i.d. = 26 mm, length = 1000 mm), which is heated by a tube furnace with a 300 mm long uniform temperature zone.

In each experiment, 1.0 g of oxygen carrier is packed at the uniform temperature zone of the quartz reactor and heated to 900 °C in air. Once the desired reaction temperature was achieved, the bed was then purged by 100 mL/min (STP) of N_2 for 5 min. After that, toluene is injected to the hot bed with a flow rate of 0.01 mL/min. The feeding time is depending on the oxygen supply coefficient. When the feeding time reached, the toluene injection pump is shut down immediately. The reaction effluent is passed through a tar sampling unit and eventually an online gas analyzer (Gasboard-3100, Cubic, China), which measured and recorded the product gas compositions. When the outlet no gases products were detected, the steam was introduced the reactor to regenerate the oxygen carrier and produce high concentration hydrogen simultaneously. The flow rate of steam is 0.01 mL/min. Each experiment is repeated three times to ensure the repeatability of the process.

2.3 Material characterization

X-ray diffraction (XRD). XRD of the OC samples was performed on an X'Pert PRO diffractometer (X'pert3 powder, PANalytical B.V., Netherlands) with Cu $K\alpha$ radiation. The 2θ range between 10° and 90° were scanned at a rate of 2°/min with a step size of 0.016°. The samples that participated in the semi in-situ XRD test in Section 3.2 were subjected to the same parameters.

Electron microscopy. The surface morphology of the OC particles was examined by scanning electron microscopy coupled with X-ray spectroscopy (SEM-EDS, X'Pert PRO, PANalytical B.V., Netherlands). High-resolution transmission electron microscopy (TEM) were determined on a JEM- ARM200F apparatus with an acceleration voltage of 200 kV.

BET/BJH analysis. The N_2 adsorption-desorption isotherms, measured by a

Micrometrics ASAP 2020 instrument. Each analysis used about 100 mg of sample, which was degassed at 300 °C for 6 h under high vacuum prior to the N_2 adsorption-desorption experiments. The specific surface area was calculated by the Brunauer-Emmett-Teller (BET) equation. The pore volumes and average pore diameters were determined using the Barrett-Joyner-Halenda (BJH) method from the desorption branch of the N_2 adsorption isotherm.

Raman spectroscopy. The Raman spectrometer (LabRAM, HR800, Horiba JobinYvon) is equipped with a 532 nm laser and measures Raman shifts from 100 cm^{-1} to 1000 cm^{-1} at room temperature. The spectrum collection time was 15 s. The measured spectra were analyzed by fitting Gaussian/Lorentzian profiles to the Raman scattering peaks.

X-ray photoelectron spectroscopy (XPS). The XPS (Axis-Ultra DLD-600W, Shimadzu-Kratos, Japan) was equipped with a monochromatic Al *Kα* X-ray source operating at 150 W (15 kV and 10 mA). The C1s peak at 285.0 eV, which corresponds to adventitious carbon, was used as an internal standard to correct for the binding energies. The analysis of the XPS spectra was done using Casa XPS. A standard Shirley background was used for all sample spectra. Following background subtraction, the surface elemental compositions of the OC samples were quantitatively analysed based on the peak areas of the binding energy peaks.

Temperature-programmed reduction (H_2-TPR) profiles. In each H_2-TPR (AutoChem II 2920, Micromeritics, USA) experiment, 200 mg of OC was placed in a U-shaped quartz tube (i.d. = 10 mm). The total gas flowrate at all stages of the H_2-TPR experiment was 100 mL/min (STP). The sample was firstly degassed and calcined by heating from room temperature to 950 °C at a rate of 10 °C/min in N_2 (99.999%), followed by 1 h of dwelling at 950 °C. Second, the sample was cooled to 50 °C, at which the gas flow was switched 10% H_2 in Ar. Then, the temperature of the sample was increased from 50 °C to 1,000 °C at a rate of 10 °C/min in10% H_2. The hydrogen consumption was quantified by measuring the outlet gas concentration using a calibrated thermal conductivity detector (TCD) analyzer.

Temperature-programmed oxidation (O_2-TPO) profiles. In each O_2-TPO (AutoChem II 2920, Micromeritics, USA) experiment, 200 mg of sample was placed in a U-shaped quartz tube (i.d. = 10 mm). where the sample was heated in 10% H_2 in He (100 mL/min) from room temperature to 950°C with a heating rate of 10 °C/min, followed by 2 h dwell at 950 °C. After that, the sample was cooled to 50 °C and hold for 5 min, at which the gas flow was switched 5% O_2 in He (100 mL/min). Then, the temperature of the sample was slowly ramped up from 50 °C to 1,000 °C at a heating rate of 10 °C/min.

Electron paramagnetic resonance spectroscopy (EPR). The photogenerated electrons and holes were investigated using EPR spectra. The EPR spectra were recorded on a Bruker A300 spectrometer at a frequency of 9.853 GHz and a sweep time of 69.456 s.

DFT Calculation. First-principles calculations were carried out using density functional theory (DFT) with generalized gradient approximation (GGA) of Perdew-Burke-Ernzerhof (PBE) implemented in the Vienna Ab-Initio Simulation Package (VASP) [17]. The valence electronic states were expanded on the basis of plane waves with the core-valence interaction represented using the projector augmented plane wave (PAW) [18] approach and a cutoff of 450 eV. The brillouin zone integration was sampled with 4×4×4 K-point meshes for bulk calculations. And adjusted to 2×2×1 for surface calculations. The structures are fully relaxed until the maximum force on each atom becomes less than 0.02 eV/Å. The climbing image nudged-elastic band (CI-NEB) algorithm was employed to identify the transition state structures for oxygen vacancy migrations [19]. The diffusion energy barriers of oxygen vacancy are calculated as the energy difference between the total energy of the transition state structures and the total energy of the initial state structures.

2.4 Data analysis

During toluene chemical looping reforming, the main gas products are CO_2, CO,

CH_4, and H_2, whereas the regeneration of the oxygen carriers produced H_2 with a small amount of CO and CO_2. Knowing that the flowrate of the N_2 carrier gas is a constant, viz. 100 mL/min, the outlet gas flow rate (F_{out}, mol/s) is calculated as:

$$F_{out} = \frac{F_{N_2}}{1-\sum x_i} \tag{1}$$

Where x_i represents the molar fraction of the gas components (i = CO_2, CO, CH_4 and H_2).

The syngas yield (Y_i, Nm^3/L) is defined as the volume of CO and H_2 produced by 1 L of toluene:

$$Y_s = \frac{22.4 \int_{t_1}^{t_2} F_{out}(x_{CO}+x_{H_2}) d_t}{V_{toluene}} \tag{2}$$

Where $V_{toluene}$ (mL) represents the total volume of toluene injected in each reforming stage. t_1 and t_2 represent the start time and end time of the reforming stage, respectively.

The time-averaged mole fraction (X_i, vol%) of species i over the entire duration of the steam toluene reforming stage is estimated by:

$$X_i = \frac{\int_{t_1}^{t_2} F_{out} x_j d_t}{\int_{t_1}^{t_2} F_{out} \sum_j x_j d_t} \times 100\% \tag{3}$$

The carbon conversion (η_C, %) is defined as the ratio of the carbon in the gas products in fuel reactor to the total carbon of toluene injected in each reforming stage:

$$\eta_C = \frac{(n_{CO}+n_{CO_2}+n_{CH_4})}{n_{toluene}^{in}} \times 100\% \tag{4}$$

Where $n_{toluene}^{in}$ is the feed amount of toluene (mol) in each experiment, and n_{CO}, n_{CO2} and n_{CH4} are the molar amounts of CO, CO_2 and CH_4 generated in fuel reactor, respectively.

Syngas purity (P_S, %) is defined as the total mole fraction of CO and H_2 in steam reactor:

$$P_S = \frac{x_{CO}+x_{H_2}}{\sum x_j} \tag{5}$$

3 Results and discussion

3.1 Characterization of $Ca_2Ni_xFe_{2-x}O_5$

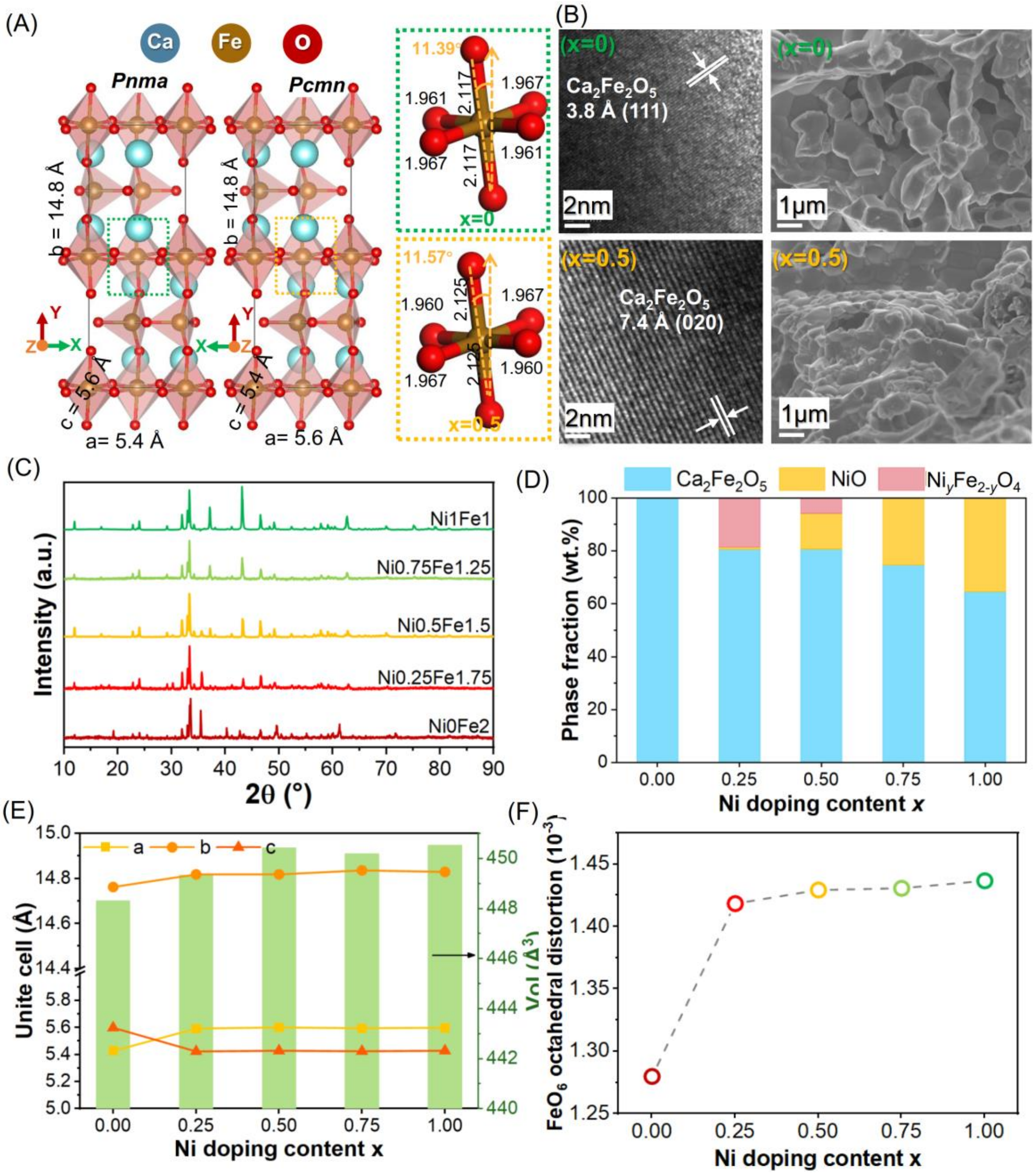

Figure 1. The composition of the as-prepared brownmillerite oxygen carriers: **(A)** crystal lattice of $Ca_2Fe_2O_5$ before and after doping, the insets show the bond lengths and degrees of distortion of the FeO_6 octahedra; **(B)** High-resolution transmission electron microscope and scanning electron microscope images of the $Ca_2Fe_2O_5$ samples. **(C)** XRD patterns; **(D)** quantitative phase analysis of the XRD patterns of the as-prepared oxygen carriers; **(E)** lattice parameters of the as-prepared oxygen carriers with different Ni contents; **(F)** FeO_6 octahedra distortion and the function of Ni doping content x.

The phase compositions of the as-prepared $Ca_2Ni_xFe_{2-x}O_5$ (x = 0, 0.25, 0.5, 0.75, 1) were studied by XRD (Figure 1C). Quantitative phase analysis were performed by Rietveld-refinement of the XRD patterns, with the results shown in Figure 1D. The full refinement results are shown in Figure S2 and Tables S1-S2. Brownmillerite phases ($A_2B_2O_5$), which consist of alternating layers of corner-sharing BO_4 octahedra and Zweier single chains of BO_4 tetrahedra (Figure 1A), are dominant in all samples. The Ni-doped brownmillerite phase, most likely by substantially doping of Ni to the BO_6 centres, exhibits reduced structural symmetry, with its space group morphing from *Pnma* (in the case of pure $Ca_2Fe_2O_5$) to *Pcmn*. While the two brownmillerite structures have similar arrangements of the BO_4 Zweier single chains, their BO_6 octahedra show different degrees of tilting along the y-axis of the primitive cubic cell: viz. 11.39° for *Pnma* and 11.57° for *Pcmn*, as depicted Figure 1A. To accommodate the extra distortion of the BO_6 octahedra, the Ni-doped brownmillerite structures underwent lattice expansion along the y-axis, with the inter layer distances increasing from 14.80 Å to 14.83 Å, as shown in Figure 1E. The experimentally measured degree of distortion, Δ is determined according to $\Delta = \frac{1}{6}\sum((R_I - R_{av}/R_{av})^2$, where R_{av} is the average bond length, and R_i is the individual bond length of Fe-O in the FeO_6 octahedra. The values of Δ are plotted as a function of Ni doping amount, as shown in Figure 1F. It can be seen that Ni doping of x = 0.25 induced a significant degree of distortion from 1.27 to 1.44, while subsequently increasing the doping amount marginally increased Δ, with Δ = 1.44 for x = 1.0. The same trend can be seen for lattice expansion, as shown in Figure 1E, indicating that FeO_6 distortion and lattice expansion are highly correlated. The experimentally measured lattice distortion and expansion can be attributed to the BO_6 octahedral centers of $Ca_2Fe_2O_5$ being occupied by Ni^{2+}, which has a larger ionic radius (0.69 Å) than Fe^{3+} (0.65 Å). Besides the distortion of the brownmillerite phase, Ni doping also resulted in the formation of minor oxide impurities. For example, $Ni_yFe_{2-y}O_4$ spinel is observed for x between 0.25 and 0.75, while NiO is observed for $0.75 < x < 1.0$. On the other hand, the formation of residual CaO-containing species as a result of the formation of $Ni_yFe_{2-y}O_4$ and NiO was not detected by XRD. We suspect that the discrepancy between the target composition and the experimentally measured composition may be due to a number of reasons, including (i) a considerable amount of calcium was lost during preparation, e.g. during sol-gel synthesis and (ii) The concentration of the residual calcium-containing species is below the detection limit of XRD and therefore cannot be determined. Nonetheless, the nature, the origin and the consequence of the residual CaO-containing species should be further investigated in follow-up studies.

The SEM of the oxygen carrier samples (Figures 1B and S3) show a random stacking of column-like crystals, which are in line with the crystal-habit of the $A_2B_2O_5$ brownmillerite structure. The high-resolution electron microscopy images (HRTEM) of the OC samples also confirm that the samples predominantly consist of brownmillerites, as reflected by the lattice fringes of 3.8 Å ($x = 0$ and $x = 1$), 3.9 Å ($x = 0.25$), 5.2 Å ($x = 0.75$) and 7.4 Å ($x = 0.5$), which correspond to the (111), (101), (110) and (020) spacings of $Ca_2Fe_2O_5$ in Figures 1F and S3.

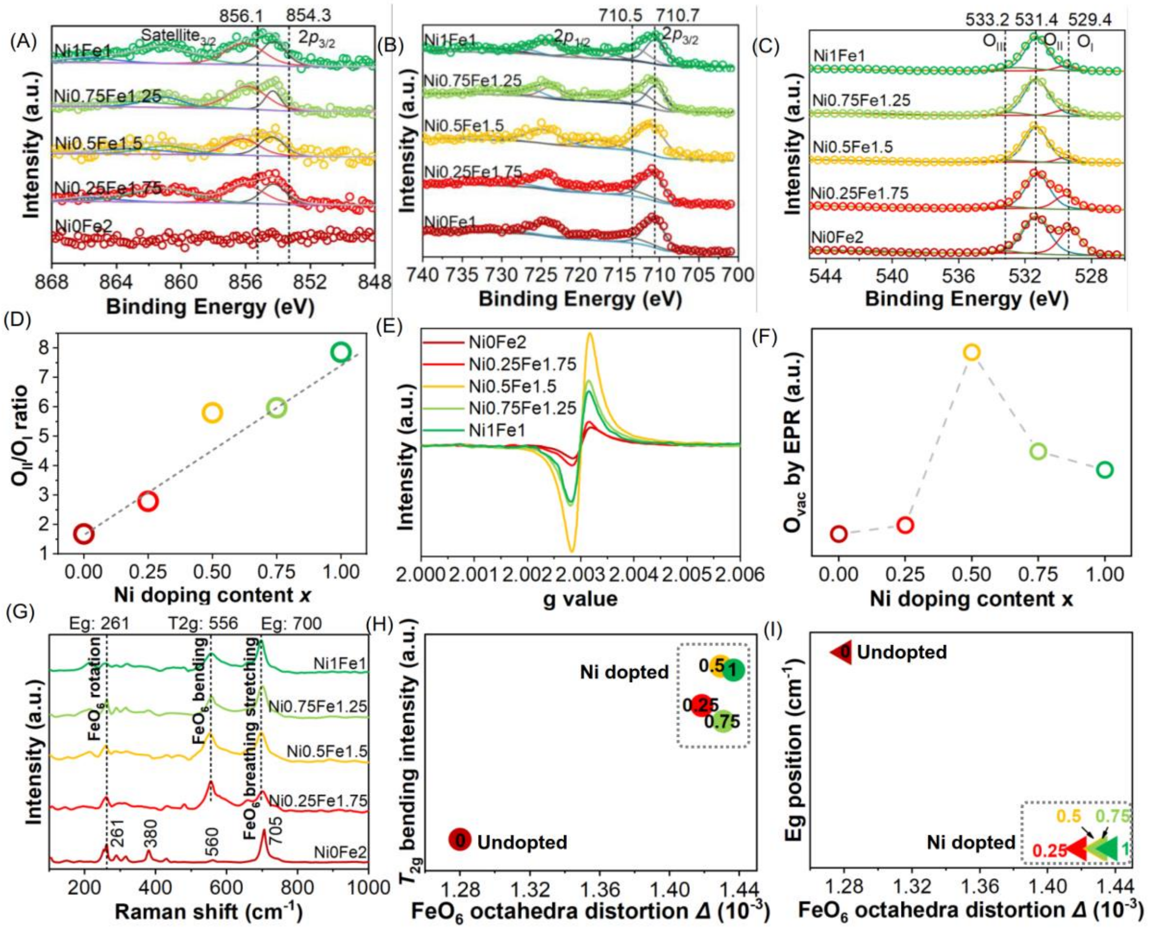

Figure 2. XPS spectra of **(A)** Ni $2p_{3/2}$, **(B)** Fe $2p$ and **(C)** O $1s$. **(D)** Plotting O_{II}/O_I ratio obtain from the O $1s$ XPS versus Ni doping content. **(E)** EPR spectra and **(F)** Oxygen vacancy obtain from the EPR versus FeO_6 octahedra Δ (10^{-3}). (G) Raman spectra and **(H)** Plotting T_{2g} bending intensity obtain from the Raman versus FeO_6 octahedra Δ (10^{-3}). **(I)** FeO_6 breathing stretching position vs FeO_6 octahedra distortion Δ (10^{-3}).

The chemical states of the as-prepared oxygen carriers and their local structures are investigated by XPS, EPR and Raman spectroscopy, as shown in Figure 2. The Ni $2p_{3/2}$ (Figure 2A and Table S3) XPS of all the Ni-doped samples can be deconvoluted to three peaks at 854.3 eV, 856.1 eV and 865.2 eV, which are assigned to Ni^{2+}, Ni^{3+}, and the satellite shake-up peak [20]. The co-existence of Ni^{2+} and Ni^{3+} suggests extensive chemical interaction between the Ni dopant and Fe-containing phases, including Ni-doped brownmillerite and Ni-Fe spinel. For $0 < x < 0.5$, the Fe $2p$ (Figure 2B) XPS is dominated by a binding energy peak at 710.7 eV, which corresponds to Fe^{3+}. As the Ni doping amount increases (i.e. $0.75 < x < 1$), a Fe $2p_{3/2}$ peak located at lower position 710.5 eV emerges, which is attributed to Fe^{2+} [21]. The formation of Fe^{2+} at high Ni doping content, *x*, suggests the partial reduction of Fe by the Ni dopant. The O 1s XPS (Figure 2C) can be decovoluted into peaks, viz., O_I: bulk lattice oxygen ~529.4 eV; O_{II}: surface absorbed oxygen ~531.4 eV; and O_{III}: surface hydroxyl or carbonate ~533.2 eV [4, 22]. In general, surface absorbed oxygen (O_{II}) are more reactive than bulk lattice oxygen (O_I). Therefore, we define the ratio O_{II}/O_I as a descriptor characterising the activity of the lattice oxygen of the oxygen carriers. It can be seen that the O_{II}/O_I ratio increases with increasing Ni doping amount (Figure 2D and Table S4), suggesting that Ni doping indeed enhances the lattice oxygen activity of the oxygen carriers.

We next examine the concentrations of oxygen vacancies (V_O) by EPR. Specifically, the EPR signal at $g = 2.003$ corresponds to the presence of lone electrons in oxygen vacancies. The EPR results (Figure 2E) show that Ni-doping promotes the formation of oxygen vacancies in the brownmillerite structure. Amongst all samples, $x = 0.5$ gave rise to the most oxygen vacancy, as shown in Figure 2F. However, further doping ($x \geq 0.75$) resulted in decreased oxygen vacancies, suggesting somewhat compromised redox activity.

The increased oxygen vacancies in the Ni-doped samples could also be related to the structural deformation of the brownmillerite phases, which could be investigated by XRD (Figure 1C) as well as Raman spectroscopy (Figure 2G). In Figure 2G, the Raman bands located between 261 cm^{-1} and 705 cm^{-1} correspond to the Ag symmetry Raman optical mode, originating from the internal vibrations of the FeO_6 octahedra in the brownmillerite structure. After Ni doping, the vibration band assigned to the T_{2g} bending of the FeO_6 octahedra, indicating increased degree of structural distortion [6]. This relationship is supported by the strong correlation between the two quantities, as shown in Figure 2H. The vibration at 261 cm^{-1} is ascribed to the E_g rotation of the Fe-O in the FeO_6 octahedra, which appears less dependent on the Ni content. Additionally, the peaks located at ~705 cm^{-1}, which are attributed to the symmetric breathing and stretching of the Fe-O bonds in FeO_6, are strongly influenced by the incorporation of Ni [23]. Upon Ni doping, the Fe-O breathing peak red-shifted to ~700 cm^{-1}, suggesting the elongation of the bond, which might be responsible for the lattice distortion (Figure 2G). The structural characterisation by Raman spectroscopy fully agrees with the structural analysis by XRD, as show in Figures 1A-E. Interestingly, while the variation of oxygen vacancy concentration with A site and B site doping has been commonly observed and extensively studied for $ABO_{3-\delta}$ ($0 < \delta < 0.5$) type perovskite structures and widely used as a strategy for turning their lattice oxygen activity [24], it was rarely investigated in-depth for $A_2B_2O_5$ brownmillerite-type oxides [14]. Based on the findings discussed above, it is apparent that the effect of B site doping to the $A_2B_2O_5$ structures is analogous to that to $ABO_{3-\delta}$ ($0 < \delta < 0.5$) structures, i.e. inducing changes in structural symmetry, bond length and bond strength of BO_6 centres, as well as the formation of lattice oxygen vacancies.

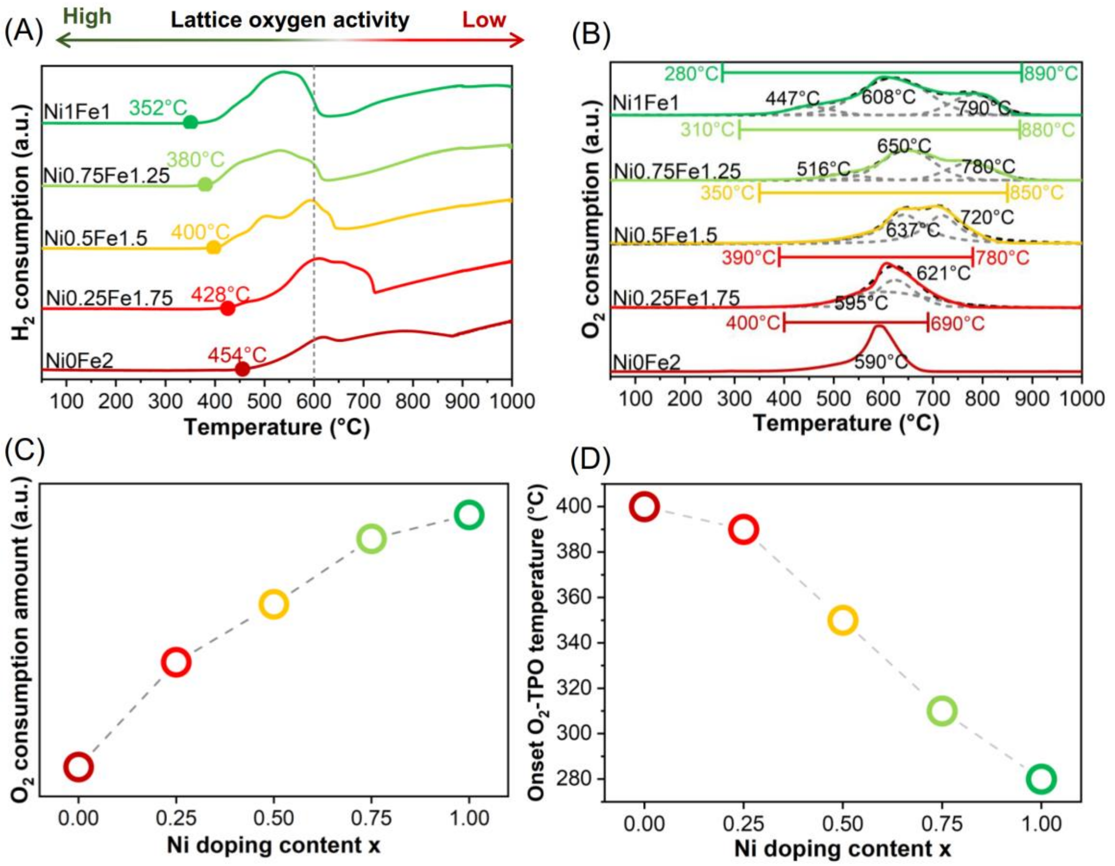

Figure 3. Redox performance of the as-prepared brownmillerite with different Ni doping content, as shown by **(A)** H_2-TPR profile; **(B)** O_2-TPO profile; **(C)** Total O_2 uptake during TPO versus Ni doping content; **(D)** the temperature in the onset O_2-TPO as a function of Ni doping content.

The redox activities of the brownmillerite-based oxygen carriers are further characterized by H_2-TPR and O_2-TPO experiments, as shown in Figure 3. For H_2-TPR of $Ca_2Ni_xFe_{2-x}O_5$, as shown in Figure 3A, the peaks at lower temperatures correspond to higher reducibility [25]. Without any doping, Ni0Fe2 started to reduce by H_2 at ~ 454 °C, and continue to reduce when temperature increases past 1,000 °C. As the Ni doping content increases, the temperatures at which OCs started to reduce decreases, with Ni1Fe1 showing the lower onset reduction temperature of 352 °C. The lowering of the reduction temperatures can be attributed to two factors: (i) Ni-doping generates more active lattice oxygen and more reducible brownmillerite phase, and (ii) metallic Ni formed upon reduction provides active sites for hydrogen spill-over, which further catalysts reduction and removal of lattice oxygen.

To elucidate the redox activities of the oxygen carriers in the absence of catalytic effects such as hydrogen spillover, pre-reduced OCs were studied by O_2-TPO, the results of which are shown in Figure 3B. For Ni0Fe2, only one peak at ~590 °C could be observed and is assigned to the regeneration of $Ca_2Fe_2O_5$ from a reduced state, possibly Fe^0. After Ni doping, more than one TPO peaks could be observed over a wider temperature range, which is typical of doped oxides [10, 26]. As the Ni content increases, the amount of oxygen taken up by the samples during TPO increases, indicating that the doping of Ni increases oxygen transfer capacity and modulates the activity of lattice oxygen, as shown in Figure 3C. Additionally, the onset oxidation temperature decreases with increasing Ni content, suggesting that the intrinsic redox activity of the Ni-doped oxygen carriers is generally enhanced (Figure 3D).

3.2 Co-production of syngas and high purity hydrogen by chemical looping steam reforming of toluene

The performance of the Ni-doped brownmillerite oxygen carriers for CLSR of toluene, a model biomass tar compound, is examined in a fixed bed reactor at 900 °C with an oxygen-supply coefficient, $\phi = 1$, which corresponds to the scenario where the supply of lattice oxygen is just sufficient to completely oxidise all the toluene to CO_2

and H_2O (i.e. $\phi = \Psi/X$, where Ψ is the lattice oxygen available for chemical looping reactions according to stoichiometry; X is the lattice oxygen required complete combustion of toluene).

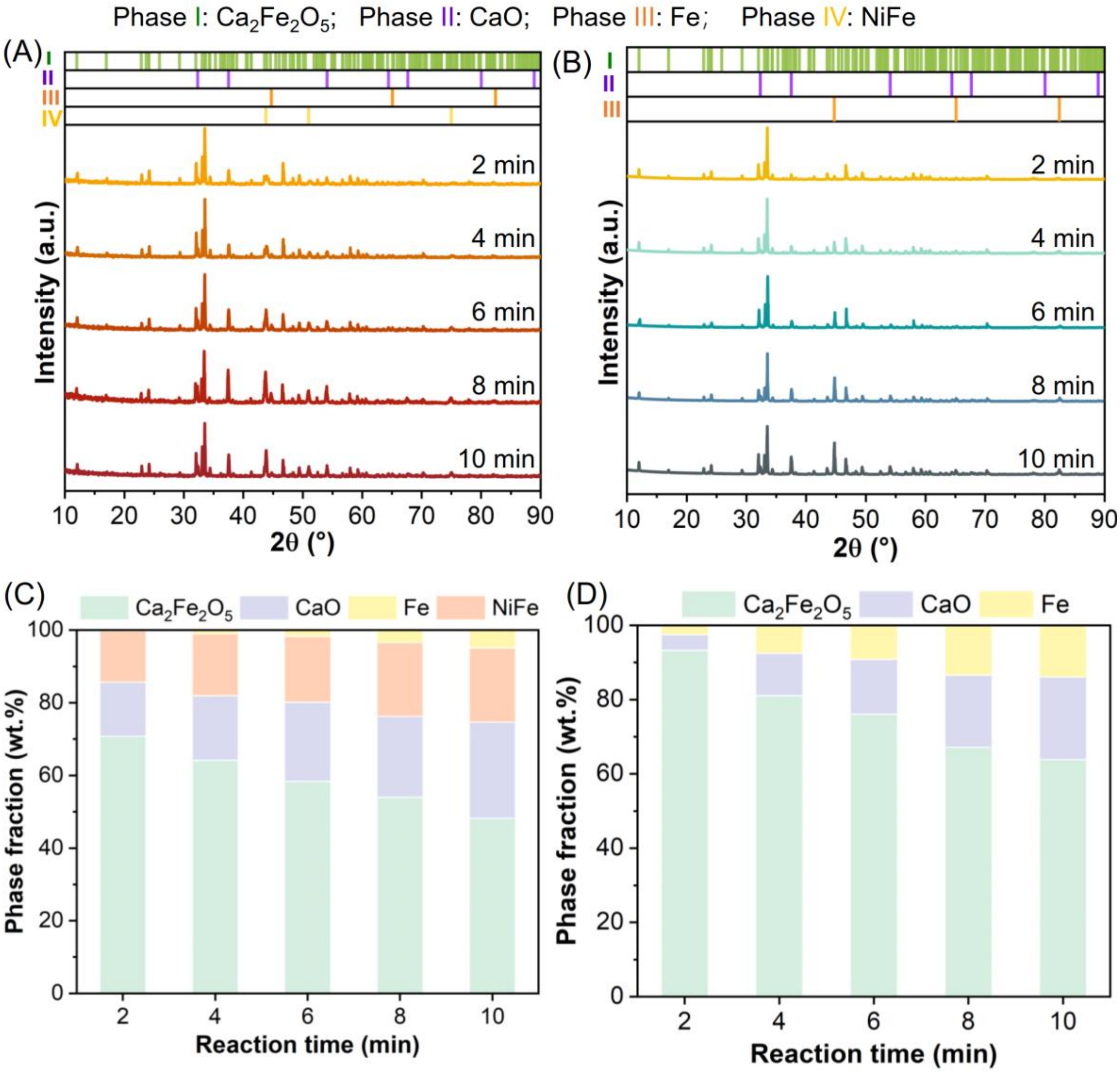

Figure 4. The structural evolution of oxygen carriers during CLSR of toluene, showing the change of XRD patterns of **(A)** $Ca_2Ni_{0.25}Fe_{1.75}O_5$ and **(B)** $Ca_2Fe_2O_5$ during the reduction stage (i.e. reactions in FR) and the results of quantitative phase analysis of the XRD patterns of **(C)** $Ca_2Ni_{0.25}Fe_{1.75}O_5$ and **(D)** $Ca_2Fe_2O_5$.

During CLSR, the oxygen carriers undergo structural evolution, which are examined by XRD of the samples collected at different stages of the reaction in FR, as shown in Figure 4. For each XRD analysis, 1.0 g of oxygen carrier was packed into the uniform temperature zone of the quartz reactor and heated to 900 °C in air. The bed was then purged by 100 mL/min (STP) of N_2 for 5 min. Toluene was subsequently injected to the hot bed with a flow rate of 0.01 mL/min. The feeding time is between 2 and 10 min (Figures 4A and 4B). At the end of the toluene feed, the toluene injection pump was turned off and the oxygen carrier was recovered from the bed after cooling to room temperature in N_2. The results of the quantitative phase analysis, performed by Rietveld-refinement of the XRD patterns (Figures 4C and 4D), showed that the undoped $Ca_2Fe_2O_5$ retained the *Pnma* space group throughout the reaction in the FR, while the doped samples kept the *Pcmn* symmetry. Upon reaction with toluene, $Ca_2Ni_{0.25}Fe_{1.75}O_5$ and $Ni_yFe_{2-y}O_4$ were gradually reduced to a mixture of nickel-iron (NiFe) alloys, metallic Fe and CaO, while that of undoped $Ca_2Fe_2O_5$ formed a mixture of Fe and CaO. Compared to undoped $Ca_2Fe_2O_5$, $Ca_2Ni_{0.25}Fe_{1.75}O_5$ exhibits enhanced oxygen carrier performance, as evidenced by the larger amounts of CaO, NiFe and Fe in the reduced sample, as well as the lower amount of $Ca_2Fe_2O_5$ phase at any given reaction time.

In addition, to verify this structural reversibility, we performed XRD and XPS analysis of the undoped $Ca_2Fe_2O_5$ and $Ca_2Ni_{0.25}Fe_{1.75}O_5$ recovered after steam oxidation, at the end of the CLSR experiment. The brownmillerite phase can be fully regenerated by steam oxidation and retains its original space group (see Figure S4), it can be seen that the effect of an additional air regeneration step on the phase composition is negligible.

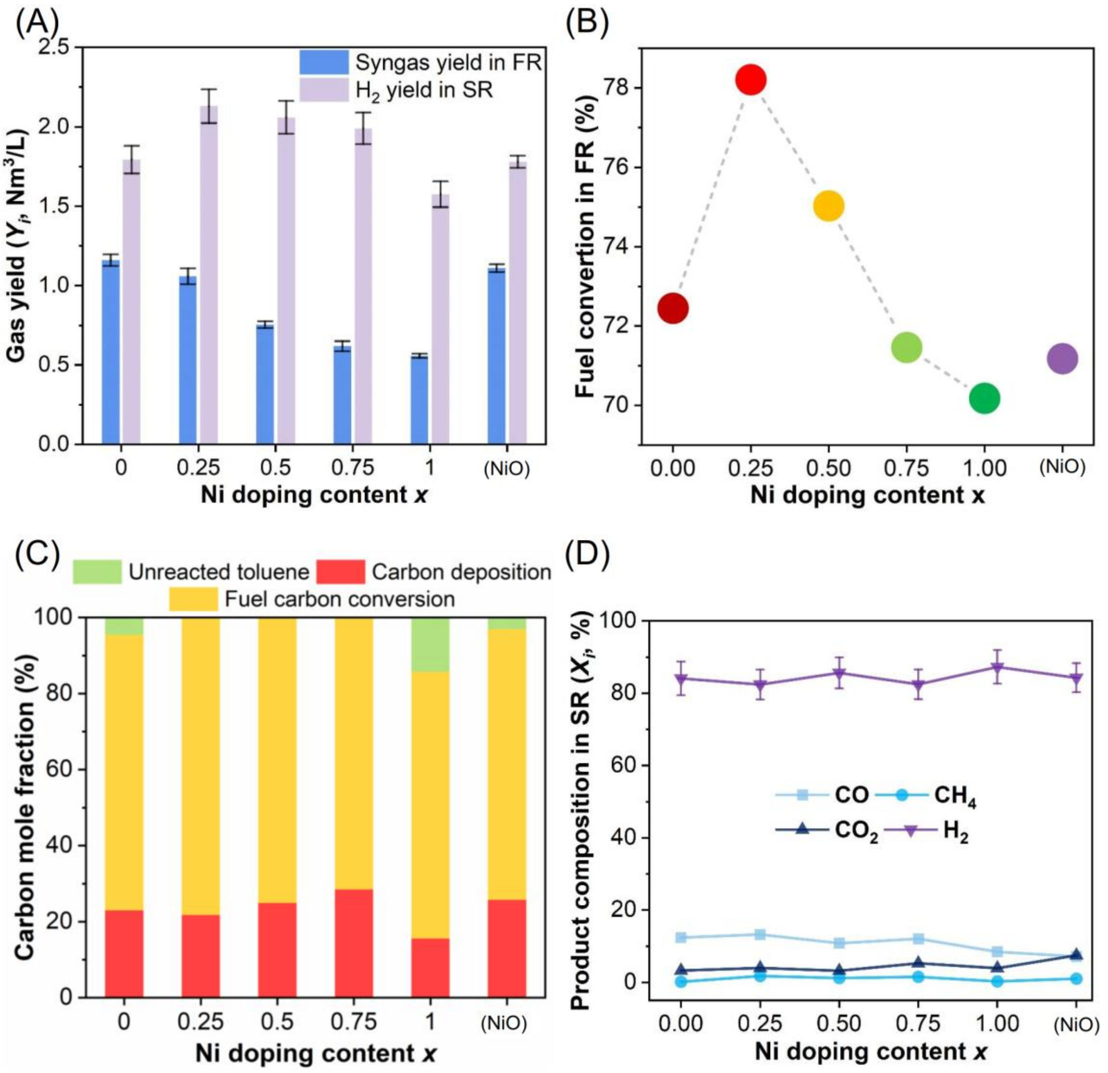

Figure 5. The performance of the various $Ca_2Fe_2O_5$ based oxygen carriers, with various extents of Ni doping for CLSR, in terms of **(A)** gas yield in the FR and AR, **(B)** fuel conversion in FR as a function of Ni doping content, **(C)** carbon distribution in FR, **(D)** product gas composition in SR. All experiments are conducted at 900 °C, with the fuel reactor supplying stoichiometric amount of lattice oxygen required for the complete oxidation of toluene ($\phi = 1$). (NiO) represents the control sample prepared by mechanically loading NiO onto $Ca_2Fe_2O_5$ with a Ni loading equivalent to $x = 0.25$.

The results of the fixed bed experiments, in terms of the production of syngas, are shown in Figure 5. In FR, toluene is oxidised by the oxygen carrier, forming a mixture of CO, CO_2, H_2 and H_2O. Owing to the design of the sampling train, all gas compositions are shown in dry basis, i.e., after complete H_2O removal. Without sufficiently active lattice oxygen, the carbonaceous species formed from the thermal cracking of toluene could not be adequately removed and subsequently polymerise, producing solid carbon and H_2, amongst other cracking products. Carbon deposition on the oxygen carriers would also be carried over to the SR, where the carbon is gasified to produce a mixture of CO and CO_2, taking place concomitantly with thermochemical water splitting by the reduced OC. Besides the thermodynamic activity, the activity of the oxygen carriers also contribute to the redox kinetics during CLSR, ultimately affecting the yields of the syngas and hydrogen in the FR and SR, respectively. Based on the analysis of the gaseous products leaving the reactors (Figure 5A), it is apparent that a doping amount of $x = 0.25$ gives rise to the most H_2 production in the SR (2.13 Nm^3/L), with the second highest amount of syngas produced in the FR (1.06 Nm^3/L), only slightly lower than the undoped $Ca_2Fe_2O_5$ (1.16 Nm^3/L). Correspondingly, $Ca_2Ni_{0.25}Fe_{1.75}O_5$ achieved the highest fuel conversion of 78.21% (Figure 5C), signifying its superior CLSR activity. The observation that $Ca_2Ni_{0.25}Fe_{1.75}O_5$ produces the highest fuel conversion but the second highest syngas yield in FR suggests that a higher fraction of toluene is converted by $Ca_2Ni_{0.25}Fe_{1.75}O_5$ to other products such as CO_2, H_2O and CH_4, than e.g. unmodified $Ca_2Fe_2O_5$, which further manifests the superior redox activity of $Ca_2Ni_{0.25}Fe_{1.75}O_5$. Further increasing the Ni doping amount resulted in reduced syngas yield and carbon conversion in FR, as well as reduced H_2 yield in SR, with $Ca_2Ni_{0.25}Fe_{1.75}O_5$ showing inferior performance of syngas yield of 0.56 Nm^3/L (Figure 5A), hydrogen yield of 1.58 Nm^3/L (Figure 5A) and fuel conversion of 70.18% (Figure 5C).

As indicated by the XRD analysis shown in Figure 4, metallic NiFe alloy and Fe would form in the FR. NiFe alloy found in the reduced $Ca_2Ni_{0.25}Fe_{1.75}O_5$ sample is generally a better alloy for activating toluene than Fe [27], which was predominately formed from the reduction of $Ca_2Fe_2O_5$ by toluene. Thus, the overall rate of syngas production in FR would depend on (1) the rate of activation of toluene on the oxygen carrier's surface, (2) the rate of supply of surface and sub-surface lattice oxygen to the activated toluene and its reaction intermediates and (3) the rate of supply of lattice oxygen from the bulk to the surface [28]. While rates 1 and 2 are influenced by the catalytic roles of the NiFe and Fe sites, rate 3 is predominately governed by the lattice oxygen activity of the bulk oxygen carrier. Therefore, a fast apparent rate of syngas production is only achievable if all three rates are sufficiently fast. Therefore, the distortion of the FeO_6 octahedra (Figure 1F) and the presence of abundant oxygen vacancies (Figure 2E) that enhance the rate of supply of lattice oxygen to the active site is directly responsible for the apparent improvement in the enhanced syngas productivity, especially when $x = 0.25$. To further verify the importance of the structural modification of the brownmillerite phase by Ni, we prepared a control sample where NiO was mechanically deposited on $Ca_2Fe_2O_5$ with loading that is equivalent to $x = 0.25$ (viz. $NiO/Ca_2Fe_2O_5$). The XRD analysis of the regenerated oxygen carrier in SR showed that complete regeneration was achieved through the regeneration of $Ca_2Fe_2O_5$ of 98.4% by steam, and retained the space group of *Pnma* (Figure S2F). Under identical operating conditions (viz. same reactor setup, same flowrates, same cyclic program, 900 °C, oxygen supply coefficient = 1), the $NiO/Ca_2Fe_2O_5$ sample afforded a H_2 yield and a fuel conversion of 1.78 Nm^3/L and 71.18%, respectively, as shown in Figures 5A and 5B. Despite the extensive presence of NiO, which could catalyse surface reactions (e.g. rates 1 and 2) after reduction and the formation of NiFe alloy, the hydrogen yield and fuel conversion of $NiO/Ca_2Fe_2O_5$ are merely comparable to those of undoped $Ca_2Fe_2O_5$ and significantly lower than those of $Ca_2Ni_{0.25}Fe_{1.75}O_5$, because the structural modification of the brownmillerite structure and the resulting high lattice oxygen activity is absent in the former. This comparison suggests that the high lattice oxygen activity is a crucial factor to the enhanced performance of $Ca_2Ni_{0.25}Fe_{1.75}O_5$ during CLSR of toluene.

Figures 5C and 5D show the product purity and selectivity of the CLSR process. In general, all oxygen carrier samples shown comparable product purity (viz. 84%) and selectivity (viz. 73%). Because of the interplay between the rate of formation of surface carbon species (e.g. by catalytic cracking of toluene on the FeNi) sites and the rate of supply of lattice oxygen from the bulk, although the enhanced lattice oxygen activity due to structural modification of the brownmillerite structure by Ni doping could substantially accelerate the rate of oxidative removal of surface carbon, the presence of exsolved NiFe sites concomitantly accelerate the generation of surface carbon species. Therefore, under the operation parameters employed in the present study, despite some marginal difference, there is no significant variation in the selectivity towards coke with the Ni doping amount.

The carbonaceous gaseous products produced in SR, viz. CO, CO_2 and CH_4, were derived from the gasification of the coke deposited on the reduced OCs. As a consequence of coking, the H_2 concertation leaving SR is compromised at ~85%. Figure 5C also shows that increasing Ni doping resulted in severe coking on the surface, this trend may be explained by the fact that excessive Ni sites has caused the rate of carbon formation to outpace the rate of supply of lattice oxygen, as discussed above. Given these results, as well as the gas yield in SR (Figure 5A) and fuel conversion in FR (Figure 5B), it can be concluded that a Ni doping amount of $x = 0.25$ affords the optimal lattice oxygen activity of the brownmillerite-based oxygen carriers to facilitate efficient fuel conversion, syngas generation and hydrogen production.

3.3 Density functional theory calculations

In this section, we rationalize the experimentally observed activity trend amongst the Ni-doped brownmillerite-based oxygen carriers using first-principle methods, i.e., density functional theory calculations. According to the XRD results (Figure 1), it is likely that Ni is substitutionally doped into the B sites of brownmillerite, replacing a Fe in a FeO_6 octahedron. It is first determined that Ni dopants are the most stable on the surface octahedral sites of $Ca_2Ni_xFe_{2-x}O_5$ than in the bulk (by 0.69 eV). Therefore, the formation energy of a surface oxygen vacancy is calculated. As shown in Figure 6A, it takes 2.38 eV to form an oxygen vacancy on the surface of undoped $Ca_2Fe_2O_5$. After Ni doping, the formation energy of an oxygen vacancy is significantly lowered to 1.45 eV, indicating that the occupancy of a surface octahedral site by Ni promotes the reducibility of the brownmillerite phase and increases the brownmillerites' capacity to host oxygen vacancies, in close agreement with the experimental characterizations shown in Figures 2 and 3. In the fuel reactor, as the lattice oxygen on the surface of the $Ca_2Ni_xFe_{2-x}O_5$ gradually depletes, an oxygen gradient develops and drives the migration of lattice oxygen from the bulk towards the surface, balanced by the migration of oxygen vacancies from the surface into the bulk. By modeling the transition state of the oxygen transport process (Figure 6D), it can be seen that the Ni-doped $Ca_2Ni_xFe_{2-x}O_5$ structure shows a significantly lower lattice oxygen diffusion barrier of 0.27 eV than an undoped system (with a diffusion barrier of 0.64 eV), as shown in Figure 6C. This reduced diffusion barrier could also explain the apparently improved reaction kinetics of the $Ca_2Ni_xFe_{2-x}O_5$ oxygen carrier, especially for $x = 0.25$ and 0.50.

The promotion of oxygen vacancy formation due to Ni doping could also be explained in terms of the change in the electronic structures of the $Ca_2Ni_xFe_{2-x}O_5$ phase, as depicted by the projected density of states (PDOS) in Figures 6B and 6C. In the brownmillerite oxide, the 3*d* orbitals of the transition metal atoms (Fe and Ni) hybridize with the 2*p* orbital of oxygen, causing orbital splitting. The hybridized orbitals participate in forming σ-bond with surface adsorbate, and can greatly influence the lattice oxygen activity [29]. In the presence of a Ni substituted surface octahedral site, the O 2*p* center shift from -2.71 eV (Figure 6C) to -1.12 eV (Figure 6B), making the number of electrons near the Fermi level decreases, which corresponds to lattice oxygen activity [29, 30]. The PDOS plots in Figures 6B and 6C also show that the Ni-doped $Ca_2Ni_xFe_{2-x}O_5$ contain Fe sites with a higher *d*-band centre of -1.55 eV than the undoped $Ca_2Fe_2O_5$ (*d*-band centre of -1.76 eV), suggesting the former is more likely to interact strongly with gaseous reactants, e.g. toluene, thereby promoting toluene activation. As the results DFT calculation and experiments suggest, Ni doping not only improves the reducibility of the $Ca_2Ni_xFe_{2-x}O_5$ oxygen carriers, but also kinetically promotes the transport of lattice oxygen through the $Ca_2Ni_xFe_{2-x}O_5$ structure and the adsorptive activation of the gaseous reactants.

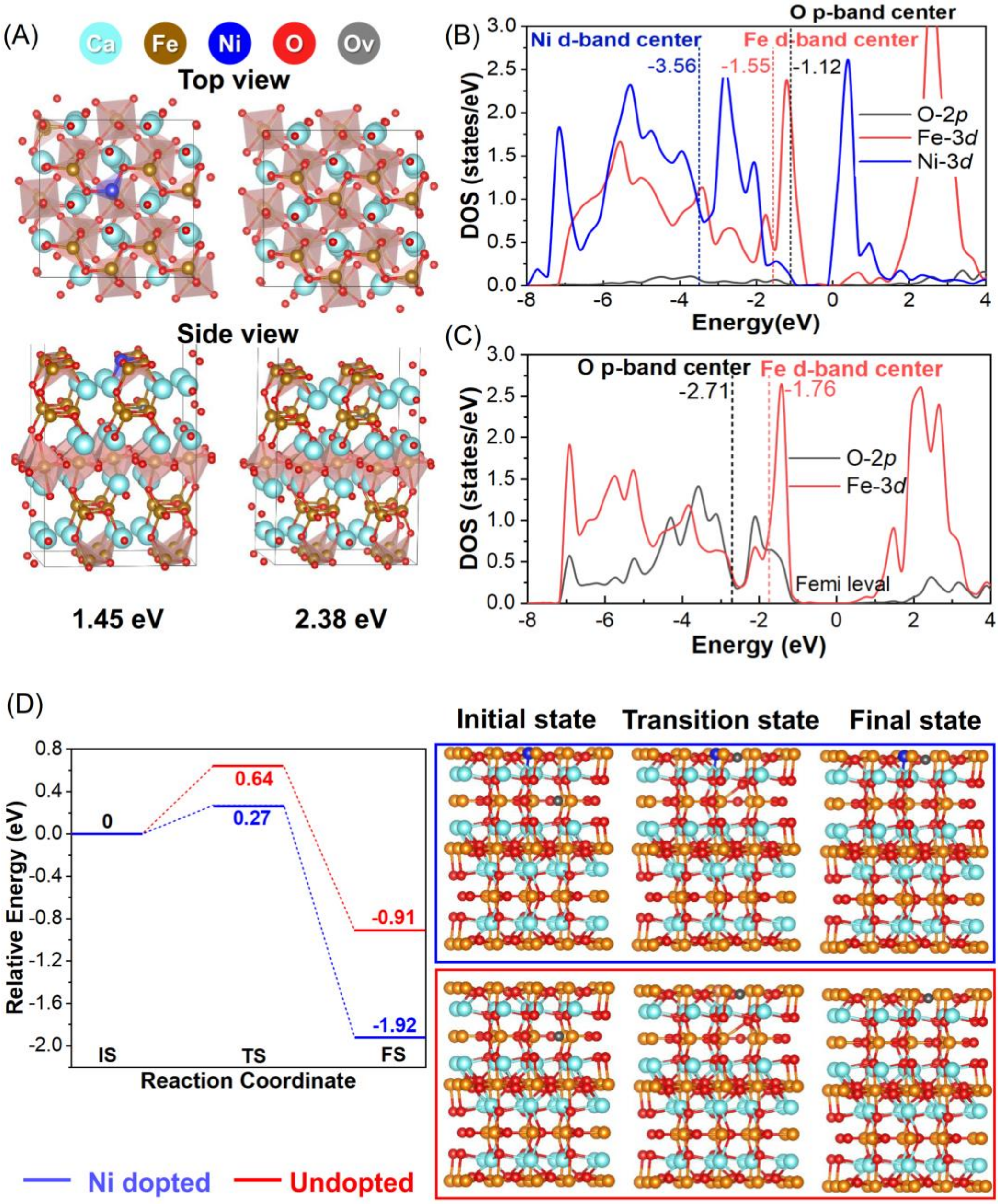

Figure 6. DFT calculation results, showing **(A)** the top and side view of the $Ca_2Fe_2O_5$ structure with an oxygen vacancy, with (Ni/Fe =1/39, i.e., $x \sim 0.05$) and without Ni doping. **(B)** and **(C)** show the calculated projected density of states of the brownmillerite phase with and without Ni doping, respectively. **(D)** The energetic pathway for the formation of an oxygen vacancy in the $Ca_2Fe_2O_5$ structures, with and without Ni doping.

4 Conclusions

We report a strategy which modulates the lattice oxygen activity of brownmillerite structured ($A_2B_2O_5$) oxygen carriers, through substitutional doping Ni to the B-sites of the brownmillerite phases. Firstly, Ni-doping resulted in structural changes, causing the symmetry of the $Ca_2Fe_2O_5$ lattice to transition from *Pnma* to *Pcmn*, as a result of increased distortion of the corner-sharing FeO_6 octahedra, whose dimension increased after partial Ni substitution. Macroscopically, Ni doping enhances the redox activity of lattice oxygen under CLSR conditions, giving rise to (i) increased thermodynamic activity of the lattice oxygen, (ii) increased rate of lattice oxygen donation and regeneration and (iii) increased surface concentration of lattice oxygen vacancies. Microscopically, Ni-doping causes the energy of oxygen vacancy formation and bulk oxygen migration to reduce from 2.38 and 0.64 eV to 1.45 and 0.27 eV, respectively, which is responsible for the apparent increase in the redox activities of the Ni-doped $Ca_2Ni_xFe_{2-x}O_5$ oxygen carriers. Ni doping also perturbs the electronic structures of the transition metal oxides, making the $Ca_2Ni_xFe_{2-x}O_5$ more active towards gaseous reactants, thereby boosting the productivity of both syngas and hydrogen in the FR and SR during CLSR. In summary, the outstanding performance of Ni-doped $Ca_2Ni_xFe_{2-x}O_5$ oxygen carriers for the coproduction of syngas and H_2 can be attributed to the increased surface oxygen vacancy concentration, accelerated migration of lattice oxygen through the oxide lattice, improved lattice oxygen activity and improved electronic structure towards stronger adsorption of gaseous reactants. With the optimal Ni doping amount of 0.25, the $Ca_2Ni_{0.25}Fe_{1.75}O_5$ oxygen carrier affords a syngas yield of 1.06 Nm^3/L a hydrogen yield of 2.13 Nm^3/L, with syngas and H_2 selectivities of 66.88% and 82.41% respectively, during CLSR in a fixed bed reactor operating at 900 °C with an oxygen supply coefficient of 1.

Acknowledgments

The research received financial support by National Natural Science Foundation of China (No. 22109048 and No. 22005112), China Postdoctoral Science Foundation (No. 2021M691121 and No. 2022T150229), and the Fundamental Research Funds for the Central Universities (No.2021XXJS040). The authors also acknowledge the

Analytical and Testing Center of Huazhong University of Science & Technology (HUST) for the analyses of the samples. The work was carried out at Shanxi Supercomputing Center of China, and the calculations were performed on TianHe-2. TX and WL acknowledge financial support by National Research Foundation under its Campus for Research Excellence and Technological Enterprise (CREATE) programme. WL also thanks Nanyang Technological University for its Start-up Grant.

References:

[1] Adanez J, Abad A, Garcia-Labiano F, et al. Progress in chemical-looping combustion and reforming technologies [J]. Progress in Energy and Combustion Science. 2012, 38(2): 215-282.

[2] Liu C, Zhao Z, Luo J, et al. Hydrogen-rich syngas production by the three-dimensional structure of $LaNiO_3$ catalyst from a blend of acetic acid and acetone as a bio-oil model compound [J]. International Journal of Hydrogen Energy. 2022, 47(34): 15160-15174.

[3] Ren J, Liu Y. Progress and prospects of produced gas utilization from biomass tar reforming [J]. Journal of Hazardous Materials Letters. 2020, 1: 100008.

[4] Li G, Li W, Xu K, et al. Sponge-like $NiCo_2O_4/MnO_2$ ultrathin nanoflakes for supercapacitor with high-rate performance and ultra-long cycle life [J]. J. Mater. Chem. A. 2014, 2(21): 7738-7741.

[5] Yu L, Zhou W, Luo Z, et al. Developing oxygen carriers for chemical looping biomass processing: Challenges and opportunities [J]. Advanced Sustainable Systems. 2020, 4(12): 2000099.

[6] Mund H S, Prajapat P, Dhaka S, et al. Impact of annealing temperature on structural, optical, and Mössbauer properties of nanocrystalline $NiFe_2O_4$ [J]. Journal of Materials Science: Materials in Electronics. 2021, 32(23): 27232-27242.

[7] Huang J, Liu W, Yang Y. Phase interactions in Mg-Ni-Al-O oxygen carriers for chemical looping applications[J]. Chemical Engineering Journal. 2017, 326: 470-476.

[8] Zhang X, Pei C, Chang X, et al. FeO_6 octahedral distortion activates lattice oxygen in perovskite ferrite for methane partial oxidation coupled with CO_2 splitting[J]. Journal of the American Chemical Society. 2020, 142(26): 11540-11549.

[9] Zhang L, Xu W, Wu J, et al. Identifying the role of A-Site cations in modulating oxygen capacity of iron-based perovskite for enhanced chemical looping methane-to-syngas conversion [J]. ACS Catalysis. 2020, 10(16): 9420-9430.

[10] Zhu Y, Tahini H A, Zhou J, et al. Tailored brownmillerite oxide catalyst with multiple electronic functionalities enables ultrafast water oxidation [J]. Chemistry of Materials. 2021, 33(13): 5233-5241.

[11] Chan M S C, Liu W, Ismail M, et al. Improving hydrogen yields, and hydrogen:steam ratio in the chemical looping production of hydrogen using $Ca_2Fe_2O_5$ [J]. Chemical Engineering Journal. 2016, 296: 406-411.

[12] Liu G, Liao Y, Wu Y, et al. Evaluation of Sr-substituted $Ca_2Fe_2O_5$ as oxygen carrier in microalgae chemical looping gasification [J]. Fuel Processing Technology. 2019, 191: 93-103.

[13] Liu G, Liao Y, Wu Y, et al. Reactivity of Co-doped $Ca_2Fe_2O_5$ brownmillerite oxides as oxygen carriers for microalgae chemical looping gasification [J]. International Journal of Hydrogen Energy. 2019, 44(5): 2546-2559.

[14] Hosseini D, Donat F, Abdala P M, et al. Reversible exsolution of dopant improves the performance of $Ca_2Fe_2O_5$ for chemical looping hydrogen production [J]. ACS Applied Materials & Interfaces. 2019, 11(20): 18276-18284.

[15] Galadima A, Masudi A, Muraza O. Catalyst development for tar reduction in biomass gasification: Recent progress and the way forward [J]. Journal of Environmental Management. 2022, 305: 114274.

[16] Xu T, Wang X, Xiao B, et al. Single-step production of hydrogen-rich syngas from toluene using multifunctional Ni-dolomite catalysts [J]. Chemical Engineering Journal. 2021, 425: 131522.

[17] Kresse G, Furthmuller J. Efficient iterative schemes for ab initio total-energy calculations using a plane-wave basis set [J]. Phys Rev B Condens Matter. 1996, 54(16): 11169-11186.

[18] Blchl P E. Projector augmented-wave method [J]. Physical review. B, Condensed matter. 1995, 50(24): 17953-17979.

[19] Henkelman G, Uberuaga B P, Jo Nsson H. A climbing image nudged elastic band method for finding saddle points and minimum energy paths [J]. The Journal of Chemical Physics. 2000, 113(22): 9901-9904.

[20] Fu Z, Hu J, Hu W, et al. Quantitative analysis of Ni^{2+}/Ni^{3+} in $Li[Ni_xMn_yCo_z]O_2$ cathode materials: Non-linear least-squares fitting of XPS spectra [J]. Applied

Surface Science. 2018, 441: 1048-1056.

[21] Gao X, Wang W, Bi J, et al. Morphology-controllable preparation of $NiFe_2O_4$ as high performance electrode material for supercapacitor [J]. Electrochimica Acta. 2019, 296: 181-189.

[22] Cao C, Guo W, Cui Z, et al. Microwave-assisted gas/liquid interfacial synthesis of flowerlike NiO hollow nanosphere precursors and their application as supercapacitor electrodes[J]. Journal of Materials Chemistry. 2011, 21(9): 3204.

[23] Sun Z, Zhang X, Li H, et al. Chemical looping oxidative steam reforming of methanol: A new pathway for auto-thermal conversion [J]. Applied Catalysis B: Environmental. 2020, 269: 118758.

[24] Dou J, Krzystowczyk E, Mishra A, et al. Perovskite promoted mixed cobalt–iron oxides for enhanced chemical looping air separation [J]. ACS Sustainable Chemistry & Engineering. 2018, 6(11): 15528-15540.

[25] Zhang L, Lin U, Yi C. Studies of Surface NiO Species in NiO/SiO, Catalysts using temperature-programmed reduction and X-ray diffraction [J]. Faraday Transactions. 1992, 88(14): 2075-2078.

[26] Zheng Y, Liao X, Xiao H, et al. Highly efficient reduction of O_2-containing CO_2 via chemical looping based on perovskite nanocomposites [J]. Nano Energy. 2020, 78: 105320.

[27] Huang J, Liu W, Yang Y, et al. High-Performance Ni–Fe redox catalysts for selective CH_4 to syngas conversion via chemical looping [J]. ACS Catalysis. 2018, 8(3): 1748-1756.

[28] Li Z. First-principles-based microkinetic rate equation theory for oxygen carrier reduction in chemical looping [J]. Chemical Engineering Science. 2022, 247: 117042.

[29] Wei C, Feng Z, Scherer G G, et al. Cations in Octahedral Sites: A Descriptor for oxygen electrocatalysis on transition-metal spinels [J]. Advanced Materials. 2017, 29(23): 1606800.

[30] Zhou S, Miao X, Zhao X, et al. Engineering electrocatalytic activity in nanosized perovskite cobaltite through surface spin-state transition [J]. Nature Communications. 2016, 7(1).